Heliyon 10 (2024) e35478

Contents lists available at ScienceDirect

Heliyon

journal homepage: www.cell.com/heliyon

Research article

Single-cell RNA-Seq reveals the heterogeneity of fibroblasts within the tympanojugular paraganglioma microenvironment☆

Shengming Wang [a,b,1], Boya Zhang [a,b,1], Zihan Lou [a,b], Yibing Hu [a,b], Jian Wang [c], Jingjing Wang [a,b,**], Zhengnong Chen [a,b,*], Shankai Yin [a,b]

[a] Otolaryngology Institute of Shanghai Jiao Tong University, China
[b] Department of Otolaryngology Head and Neck Surgery, Shanghai Sixth People's Hospital Affiliated to Shanghai Jiao Tong University School of Medicine, Shanghai, China
[c] School of Communication Sciences and Disorders, Dalhousie University, Halifax, NS, Canada

ARTICLE INFO

Keywords:
Single-cell RNA sequencing
Fibroblast diversity
Cell–cell interaction
Transcriptomic atlas
Paragangliomas

ABSTRACT

Tympanojugular paragangliomas (TJP) originate from the parasympathetic ganglia in the lateral base of the skull. Although the cellular composition and oncogenic mechanisms of paragangliomas have been evaluated, a comprehensive transcriptomic atlas specific to TJP remains to be established to facilitate further investigations. In this study, single-cell RNA sequencing and whole-exome sequencing were conducted on six surgically excised TJP samples to determine their cellular composition and intratumoral heterogeneity. Fibroblasts were sub-classified into two distinct groups: myofibroblasts and fibroblasts associated with bone remodeling. Additionally, an elaborate regulatory and cell–cell communication network was determined, highlighting the multifaceted role of fibroblasts, which varies depending on expression transitions. The Kit receptor (KIT) signaling pathway mediated interactions between fibroblasts and mast cells, whereas robust connections with endothelial and Schwann cell-like cells were facilitated through the platelet-derived growth factor signaling pathway. These findings establish a foundation for studying the mechanisms underlying protumor angiogenesis and the specific contributions of fibroblasts within the TJP microenvironment. IL6 signaling pathway of fibroblasts interacting with macrophages and endothelial cells may be involved in tumor regrowth. These results enhance our understanding of fibroblast functionality and provide a resource for future therapeutic targeting of TJP.

☆ The authors have declared that no conflict of interest exists.

* Corresponding author. Otolaryngology Institute of Shanghai Jiao Tong University, Department of Otolaryngology Head and Neck Surgery, Shanghai Sixth People's Hospital Affiliated to Shanghai Jiao Tong University School of Medicine, No. 600 YiShan Road, XuHui District, Shanghai City, China.

** Corresponding author. Otolaryngology Institute of Shanghai Jiao Tong University, Department of Otolaryngology Head and Neck Surgery, Shanghai Sixth People's Hospital Affiliated to Shanghai Jiao Tong University School of Medicine, No. 600 YiShan Road, XuHui District, Shanghai City, China.

E-mail addresses: wjjrebecca@126.com (J. Wang), jassey@126.com (Z. Chen).

[1] Co-first authors.

https://doi.org/10.1016/j.heliyon.2024.e35478
Received 21 July 2024; Accepted 29 July 2024
Available online 31 July 2024
2405-8440/© 2024 The Authors. Published by Elsevier Ltd. This is an open access article under the CC BY-NC-ND license (http://creativecommons.org/licenses/by-nc-nd/4.0/).

1. Introduction

Paragangliomas (PGLs) are tumors originating from the sympathetic or parasympathetic ganglia, most of which are endocrine-active [1]. Head and neck PGLs (HNPGLs) constitute approximately 3 % to 7–16 % [2] of all PGLs and are characterized by high heterogeneity [3]. The proportion of hereditary cases of HNPGLs is notably high (approximately 33–50 %), and susceptibility genes associated with hereditary HNPGL include succinate dehydrogenase (SDH) subunit genes (most commonly *SDHD* and *SDHB*) or SDH assembly factors, with *SDHB* mutations showing a propensity for malignant metastasis. Tympanojugular paragangliomas (TJPs) account for approximately 30 % of all HNPGLs and are among the most common tumors in the middle ear and temporal bone; TJPs cause pulsatile tinnitus, hearing loss, and/or lower cranial nerve damage [4,5]. Surgical resection is the recommended treatment for non-metastatic and limited PGLs, but the anatomical proximity to the lateral skull base typically makes the surgery, particularly for TJPs, challenging and prone to complications [6]. Further investigation of the transcriptomic characteristics of TJP is necessary to optimize treatment strategies.

Immunohistochemistry (IHC) and single-nucleus RNA sequencing (RNA-seq) have been used to identify fibroblasts in PGL. Fibroblasts promote tumorigenesis through various potential mechanisms, including promoting tumor growth and metabolism, facilitating metastasis and angiogenesis, and establishing an inflammatory microenvironment. In PGL, fibroblasts promote tumorigenesis via the promotion of tumor cell anchoring, migration, and metabolism [7,8]. Co-culture of fibroblasts and pheochromocytoma cell lines demonstrated that lactate secreted by fibroblasts specifically enhances tumor cell migration in *SDHB*-silenced tumors [9]. Furthermore, the migration ability of SDHB-silenced tumor spheroid cells is proportional to the abundance of fibroblasts and exceeds that of SDHD-silenced tumor spheroid cells, whereas a low-glucose environment affects tumor invasiveness by influencing fibroblast metabolism.

The complexity and heterogeneity of fibroblasts have been elucidated at single-cell resolution across multiple tumor types. As part of the connective tissue adjacent to the tumor, fibroblasts are considered an important cellular component of the tumor microenvironment of PGLs [10,11]. Although histopathological methods [12] and single-nucleus RNA-seq have been used to identify the cellular components of this disease, histopathological techniques do not provide transcriptomic information, and single-nucleus RNA-seq is limited to analysis of the cell nucleus; in contrast, single-cell RNA-seq (scRNA-seq) [13] can be used to evaluate the cytosol. Therefore, in this study, scRNA-seq was used to evaluate six TJPs and 63,765 cells. The dynamic characteristics of heterogeneity within 25,294 TJP fibroblasts and intricate cell interactions within the tumor microenvironment were comprehensively evaluated.

2. Material and methods

2.1. Tumor specimens from patients with TJP

Six patients who were pathologically diagnosed with TJP using scRNA-seq at the Department of Otolaryngology, Shanghai Jiao Tong University Affiliated Sixth People's Hospital were recruited for this study. All patients underwent stenting of the internal carotid artery for preoperative precautions at 24–48 h prior to surgery. None of the patients received antitumor therapy. The tumor was primary in five patients and one was reoccurred. Demographic information was collected before surgery and presented in Table 1. Half tissue of each specimen was used for scRNA-Seq, and the other half was for multiplex immunohistochemistry (mIHC), and whole-exome sequencing.

2.2. Hydrolysis of tumor samples

The half tissue for scRNA-seq from each sample was rinsed twice with cold saline, cut into ~1–2 mm^3 pieces, and digested using a Solo™ Tumor Dissociation Kit (Sinotech Genomics, Shanghai, China, Cat# JZ-SC-58201) at 37 °C for 30–60 min. Enzymatic digestion was stopped by adding excess RPMI-1640 medium, and the cells were filtered through a 40 μm cell strainer. The single-cell solution was kept on ice before loading onto a BD Rhapsody cartridge (BD Biosciences, Franklin Lakes, NJ, USA) for single-cell transcriptome capture.

2.3. Single-cell transcriptome capture, library construction, and sequencing

The isolated single cells were first stained with two fluorescent dyes, Calcein AM for cell concentration and Draq7 for cell viability

Table 1
General information of the samples.

Patient Number	Gender	Age (yr)	Diagnosis	Tumor Size(cm)	Fisch Classification	SDHx Mutation	Regrowth
1	Male	28	Right TJP	3.4*3.3*3.6	**C4, Di2**	**SDHD**	**Yes**
2	Male	35	Left TJP	3.3*2.8*3.6	**C2, Di1**	**SDHC**	**No**
3	Female	55	Right TJP	3.1*2.3*3.2	**C1, De1**	**SDHC**	**No**
4	Female	48	Left TJP	1.2*1.7*1.5	**C1**	**NA**	**No**
5	Male	49	Left TJP	3.4*3.2*3.1	**C3, Di1**	**NA**	**No**
6	Male	49	Right TJP	2.2*2.0*1.9	**C2**	**NA**	**No**

respectively. The stained cells were loaded into one BD Rhapsody™ Scanner (BD Biosciences). Subsequently, the cells were loaded into one BD Rhapsody microwell cartridge as described by Fan et al. [14]. Excessive cell capture beads were loaded to ensure that nearly every microwell contained one bead. The excess beads were washed away from the cartridge. After lysis buffer was added, the cell capture beads were retrieved and washed prior to reverse transcription. The microbead-captured single-cell transcriptome was generated as a cDNA library containing cell labels and unique molecular identifiers (UMI). All procedures were performed using a BD Rhapsody cDNA Kit (BD Biosciences, Cat. No. 633773) and BD Rhapsody Targeted mRNA & AbSeq Amplification Kit (BD Biosciences, Cat No. 633801) according to the manufacturer's protocol. All libraries were sequenced in PE150 mode (pair-end for 150 bp read) on a NovaSeq platform (Illumina, San Diego, CA, USA).

2.4. Sequencing data processing

Raw sequencing reads of the cDNA library were processed using the BD Rhapsody Whole Transcriptome Assay Analysis Pipeline (v1.8), which included filtering by read quality, annotating reads and molecules, determining putative cells, and generating a single-cell expression matrix. Among all output files, the Matrix of UMI counts for each gene per cell was used for downstream analysis. Genome Reference Consortium Human Build 38 (GRCh38) was used as a reference for the BD pipelines.

2.5. Single-cell expressing matrix pretreatment

After processing the sequencing data, the matrix of UMI counts in each gene per cell for each sample was visualized using the Seurat (v4.0.0) pipeline in R (v 4.0.5).

Briefly, the UMI data were first log-normalized using NormalizeData (Seurat R Package) according to the UMIs in each cell and then transformed to a log scale with a scale factor of 10^4. Cells with >25 % mitochondrial UMI, <500 UMI, or 200 genes were excluded from the dataset. The most variable genes were selected using FindVariableGenes (Seurat R Package) using default parameters. The top 30 principal components were chosen using RunPCA (Seurat R Package) to construct a shared nearest-neighbor graph. To examine specific gene expression correlations within the data, we used the AddModuleScore (Seurat R Package) to determine the expression score.

2.6. Batch correction and multiple dataset integration

Harmony algorithm (v1.0) was used to minimize the batch effect when merging datasets from different sources and samples [15]. An updated Seurat object was returned using RunHarmony (Harmony R Package). The latter clustering and visualization were based on corrected Harmony embeddings within the updated Seurat object rather than on principal components.

2.7. Dimensionality reduction, clustering, and visualization

After testing different resolution parameters, we opted for a resolution of 0.8 to improve clustering accuracy. Clustering was performed using graph-based clustering and visualized using *t*-distributed stochastic neighbor embedding or uniform manifold approximation and projection with RunTSNE and RunUMAP (Seurat R Package). Feature plots, violin plots, and heatmaps were used to visualize the expression of genes or gene sets within each cluster.

2.8. Cell cluster annotation

FindMarkers (Seurat R Package) was used to identify specific markers for each cluster. To identify cell types in the filtered sample datasets in an unbiased manner, we used SingleR (v1.4.1), a computational framework that refers to bulk transcriptomes [16] to annotate the cell type for each cluster. The Human Primary Cell Atlas was used as the reference dataset [17]. Adjustments were made according to the biological backgrounds of the patients.

2.9. Enrichment analysis and pseudotime trajectory analysis

By using FindMarkers in Seurat Package, differentially expressed genes between specific cell clusters were obtained. ClusterProfiler (v4.0.5) was used for Gene Ontology (GO) pathway enrichment and annotation [18]. After cluster annotation, all fibroblast subsets were separated from the single-cell dataset and subjected to a similar analysis. Monocle3 (v1.0.0) was used to obtain a pseudotime trajectory [19].

2.10. Transcription factor regulation network analysis

The scRNA-seq data were included in single-cell regulatory network inference and clustering (SCENIC) analysis (v1.2.2) [20] and sorted by cell type and cluster. Genes that were not included in the RcisTarget database (https://resources.aertslab.org/cistarget) were excluded. Using GENIE3 (SCENIC R Package) [21], the association between transcription factors (TFs) and possible targets in the dataset were detected, and the gene regulatory network was reconstructed. The v9 cisTarget Human Motif database (https://resources.aertslab.org/cistarget/motif2tf/motifs-v9-nr.hgnc-m0.001-o0.0.tbl) was used for *cis*-regulatory motif analysis.

RunSCENIC_4_aucell_binarize (SCENIC R Package) was used to determine the enrichment of regulons across single cells. The SCENIC analysis results were incorporated into the Seurat object as metadata for further analysis. Additionally, *t*-distributed stochastic neighbor embedding clustering was performed based on the area under the curve matrices of the regulons.

2.11. Cell–cell communication analysis

Cell–cell communication refers to the interaction between different cell types through secreted signals, extracellular matrix-receptors, or cell–cell contact. Ligand–receptor interactions among different cell groups were inferred using CellChat (v1.6.0), a publicly available database of curated receptors, ligands, and their interactions.

2.12. Whole-exome sequencing

All specimens for whole-exome sequencing were obtained from surgically resected formalin-fixed paraffin-embedded tissues, and 3 μm × 10 sections of tumor tissues were prepared for DNA extraction (excluding the NO.1 blood test). DNA was extracted using a QIAamp DNA FFPE Tissue Kit (Magen Biotechnology Co., Ltd., Guangzhou, China, Cat# D6323-02B). Genomic DNA was sheared randomly into 180–280 bp fragments using sonication (Covaris, Woburn, MA, USA). A DNA library was constructed using a Rapid CE DNA Lib Prep Kit Illumina V2 (RK20254, ABclonal, Woburn, MA, USA). Human whole-exon DNA enrichment was performed using an xGen Exomeesearch Panel v 2.0 (Integrated DNA Technologies, Coralville, IA, USA), followed by the preparation of DNA sequencing libraries. The AMPure XP system (Beckman Coulter, Brea, CA, USA) was applied to purify the PCR products, and the size distribution of the libraries was analyzed using a 2100 Bioanalyzer (Agilent Technologies, Santa Clara, CA, USA) and quantified using qPCR (3 nM). The DNA libraries were sequenced on an Illumina Hiseq platform according to the manufacturer's protocol, and raw reads were obtained. The target sequencing depth of tumor tissues was 900×.

Raw data were filtered as follows: identification of reads with adapter deletion; deletion of reads containing more than 10 % unrecognized base information; and removal of paired reads when low-quality (<5) bases of single-ended reads exceeded 50 % in length. The filtered data were aligned to obtain the BAM file by Burrows-Wheeler Aligner and Samblaster [22]. Data were filtered using Samtools, Picard and GATK, local realignment, recalibration to give the final BAM file [23].

2.13. mIHC

mIHC was performed by sequentially staining 4-μm-thick formalin-fixed, paraffin-embedded whole tissue sections with standard primary antibodies and processing using a 7-color IHC Kit (abs50015-100T, Absinbio, China). Deparaffinized slides were incubated with a primary antibody for 30 min and then treated with an anti-rabbit/mouse horseradish peroxidase-conjugated (HRP) secondary antibody for 10 min. Labeling was performed for 10 min using TSA 520 according to the manufacturer's instructions. Slides were washed in Tris-buffered saline containing Tween 20, transferred to a preheated citrate solution (90 °C), and heat-treated in a microwave set at 20 % maximum power for 15 min. The slides were cooled in the same solution to room temperature. After each step, the slides were washed with Tris buffer. This process was repeated. Each slide was treated with two drops of DAPI (D1306, Thermo Fisher Scientific, Waltham, MA, USA), washed in distilled water, and manually covered with a slip. The slides were air-dried, and images were captured using an Aperio Versa 8 tissue imaging system (Leica, Wetzlar, Germany). Images were analyzed using Indica Halo software and QuPath software (v0.5.0) [24]. Antibodies used for mIHC are listed in Supplemental Table 1.

2.14. Cell counting

The digitized slides were analyzed using QuPath (v0.5.0). Regions randomly selected at 60× magnification were examined, and a cell detection tool was used for cell counting. ACTA2-positive cell counts were performed based on the antibody labeling using the appropriate object classifier.

2.15. Antibodies

The following antibodies were used in this study: S100 beta polyclonal antibody (15146-1-AP), transgelin/SM22 polyclonal antibody (10493-1-AP), PDAP1 polyclonal antibody (15081-1-AP), Sortilin polyclonal antibody (12369-1-AP), and APOD monoclonal antibody (66215-1-Ig) from Proteintech (Rosemont, IL, USA); CD34 rabbit pAb (A0761), SMMHC/MYH11 Rabbit mAb (A4064), CD117/c-Kit rabbit pAb (A0357), KITLG rabbit pAb (A16245), TPSAB1 rabbit pAb (A2022), PDGFRB rabbit pAb (A1444), granulin rabbit pAb (A12440), and synapsin-1 rabbit mAb (A24122) from ABclonal; PDGFRA antibody (38364) from Signalway Antibody (Greenbelt, MD, USA); anti-α-SMA antibody (monoclonal, 1A4) (BM0002) from BOSTER (Wuhan, China); anti-lumican antibody (ab168348) from Abcam (Cambridge, UK); Cy3-conjugated goat anti-rabbit IgG (GB21303), Cy3-conjugated goat anti-mouse IgG (GB21301), Cy3-conjugated goat anti-rat IgG (GB21302), Cy3-conjugated donkey anti-goat IgG (GB21404), Cy3-conjugated donkey anti-mouse IgG (GB21401), Cy3-conjugated donkey anti-rabbit IgG (GB21403), Alexa Fluor 488-conjugated goat anti-rabbit IgG (GB25303), Alexa Fluor 488-conjugated goat anti-mouse IgG (GB25301), Cy5-conjugated goat anti-mouse IgG (GB27301), Cy5-conjugated goat anti-rabbit IgG (GB27303), HRP-conjugated rabbit anti-goat IgG (GB23204), HRP-conjugated goat anti-mouse IgG (GB23301), HRP-conjugated goat anti-rat IgG (GB23302), HRP-conjugated goat anti-rabbit IgG (GB23303), HRP-conjugated donkey anti-goat IgG (GB23404), FITC-conjugated donkey anti-goat IgG (GB22404), FITC-conjugated goat anti-rat IgG (GB22302), FITC-

conjugated donkey anti-rabbit IgG (GB22403), FITC-conjugated donkey anti-mouse IgG (GB22401), FITC-tyramide (G1222), CY3-tyramide (G1223), iF488-tyramide (G1231), and iF647-tyramide (G1232) from Servicebio (Wuhan, China); and Alexa Fluor 594-conjugated goat anti-rabbit IgG (111-585-003) and Alexa Fluor 594-conjugated goat anti-mouse IgG (115-585-003) from Jackson Laboratories (Bar Harbor, ME, USA).

2.16. Statistical analysis

For Seurat objects, characteristic genes for each subgroup were calculated using FindMarkers (Seurat R package), along with statistical analysis using Wilcoxon rank-sum test and correction using Bonferroni multiplex test [25]. For enrichment analysis, hypergeometric distribution tests, also known as Fisher's exact tests, were used to identify significantly enriched biological terms using ClusterProfiler (v4.0.5) [18].

3. Results

3.1. Cellular composition of TJP in six patients

TJP tumor samples from six patients, all presenting with unilateral tumors classified as Fisch C, were subjected to scRNA-seq to investigate their transcriptomic characteristics at single-cell resolution (Fig. 1A). Each sample met the quality control standards for cell concentration, viability, cell retention rate, and bead retrieval efficiency. Following filtering based on cell status and the removal of potential doublets, 47,883 cells were obtained and analyzed.

After stringent initial filtering, scRNA-seq data were processed and visualized using uniform manifold approximation and projection analysis. Based on previous studies, cell clusters were categorized into nine main types (Fig. 1B). The main marker genes of each

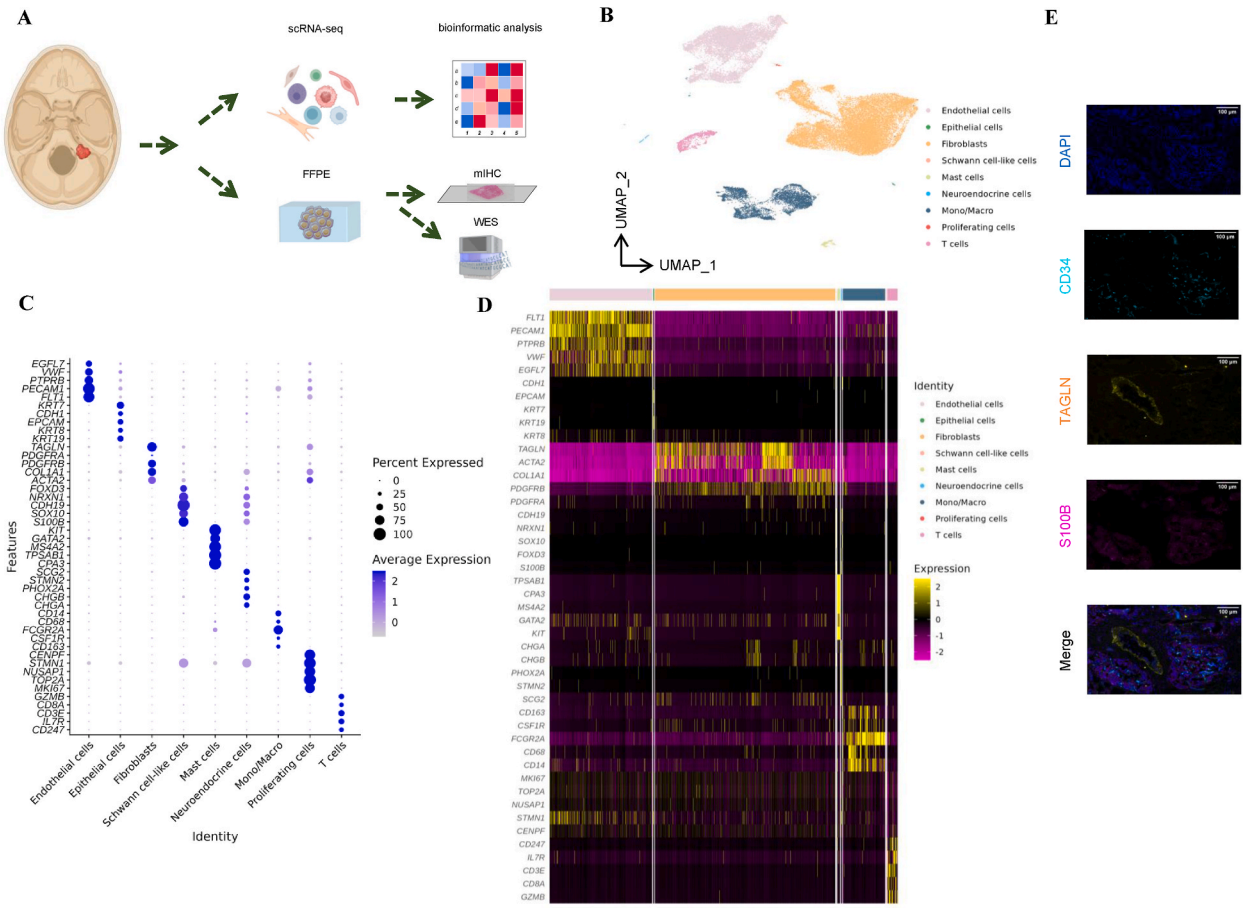

Fig. 1. Single-cell transcriptomic atlas of TJP A. Schema showing the workflow of this study. (Created with BioRender.com.) B. UMAP embeddings of 47883 cells from 6 patients and the main cell types. C. Dot plot of main cell markers for each cell type according to the previous research. D. Heatmap of the expression of those characteristic genes of the nine main cell types. E. H&E staining and mIHC of the pathological sections. (Scale bar: 100 μm).

cell type were classified as follows: endothelial cells exhibiting high expression levels of *EGFL7*, *VWF*, *PTPRB*, *PECAM1*, and *FLT1* [8, 26]; epithelial cells showing high expression of *EPCAM* [27], *KRT7* [28], *KRT8* [29], *CDH1*, and *KRT19* [30]; fibroblasts specifically expressing *TAGLN*, *ACTA2*, *COL1A1* [26], *PDGFRA* [27], and *PDGFRB* [8]; Schwann cell-like cells characterized by the expression of *PLP1* [31], *SOX10*, *FOXD3*, *S100B* [32], *SOX6*, and *CDH19* [26]; proliferating cells displaying high expression of *MKI67*, *TOP2A* [33, 34], *TUBB*, *STMN1*, and *CENPE* [35]; mast cells highly expressing *TPSAB1*, *CPA3* [8,36], *MS4A2*, *GATA2*, and *KIT* [37]; monocytes/macrophages exhibiting high expression levels of *CD163*, *CSF1R*, *TGFBI* [26], *CD14*, and *CD68* [38]; neuroendocrine cells specifically expressing *CHGB* [26], *CHGA*, *PHOX2A*, *STMN2* [39], and *SCG2* [40]; and T cells characterized by the expression of *CD247*, *IL7R*, *TCF7*, *CD3E* [26], and *GZMB* [8] (Fig. 1C and D, Supplemental Fig. S1A). The proportion of each cell type varied substantially among different samples, indicating intertumoral heterogeneity in TJPs. However, fibroblasts constituted the largest proportion (52.82 %) among the cell types. mIHC staining confirmed the positive expression of markers for *CD34*, *S100B*, and *TAGLN* in pathological sections, validating the results of the differentially expressed genes (Fig. 1E). Markers for *SYN*, *S100B*, *ACTA2*, and *LUM* were employed to examine the spatial distribution of fibroblasts and neuroendocrine cells (Supplemental Fig. S1B), and immunostaining revealed that the proportion of ACTA2-positive cells was approximately 32 %.

These scRNA-seq results revealed the comprehensive cellular composition of TJP and provided a detailed and informative landscape.

3.2. Heterogeneity of fibroblasts

The results indicate that fibroblasts play a key role in the TJP microenvironment, which is consistent with previous studies. Fibroblasts data were separated from the entire dataset for further investigation and re-clustered into nine distinct clusters (Fig. 2A). Over 96 % of the data comprised clusters Fib_0 (45.3 %), Fib_1 (20.1 %), Fib_2 (11.2 %), Fib_3 (10.1 %), Fib_4 (5 %), and Fib_5 (4.4 %), characterized by the specific marker genes, *AKAP12, JUN, MYH11*, *LUM*, *IGFBP5,* and *CCL2,* respectively (Supplemental Figs. S2A and S2B). Fib_0, Fib_1, Fib_2, Fib_4, and Fib_5 were further defined as myofibroblasts according to their high expression of *ACTA2*, *MYL9*,

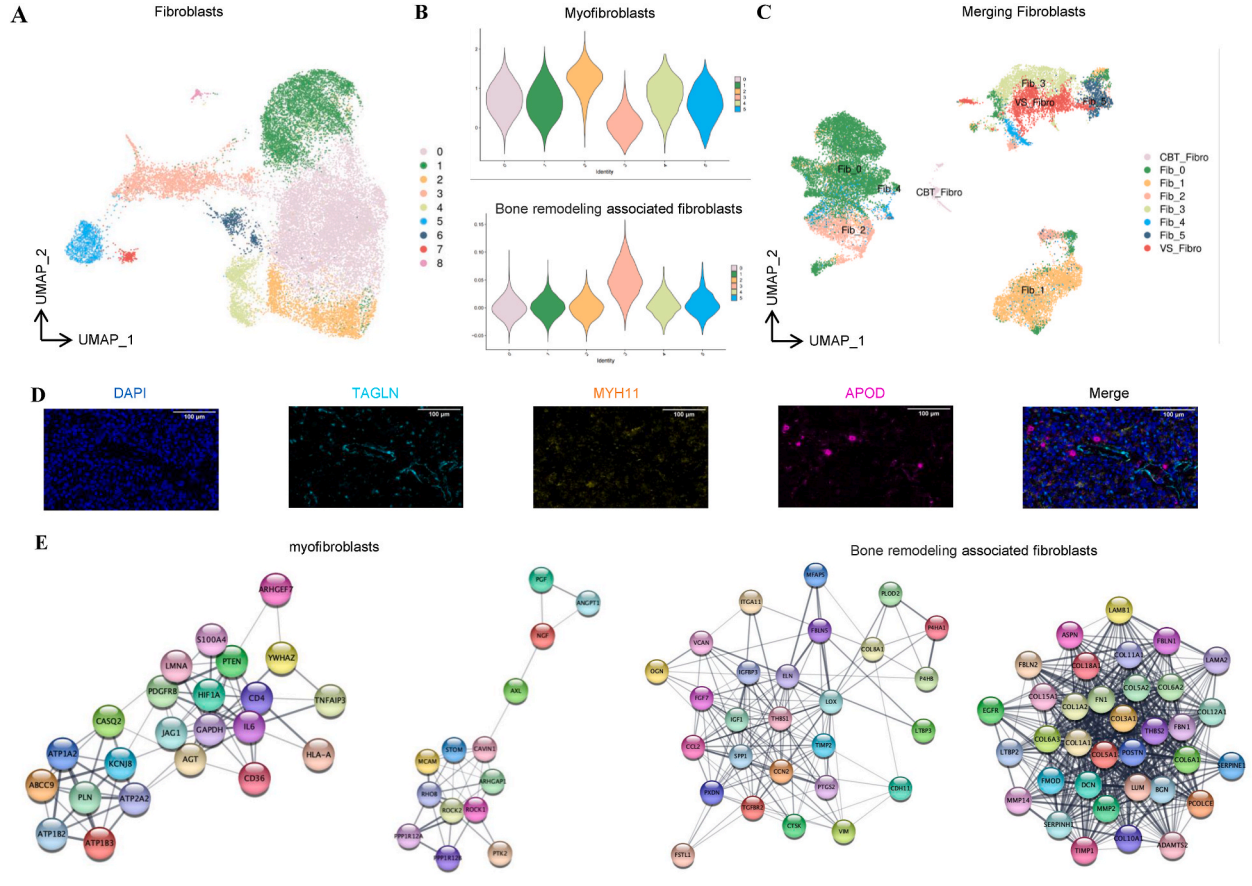

Fig. 2. Heterogeneity of fibroblasts in TJP A. UMAP embeddings of 25294 fibroblasts from the overall scRNA-seq data. B. Vlnplot showing the vascular gene set score and bone remodeling related GO pathway score in the six main fibroblasts subgroups. C. Embedding of the merged data for fibroblasts from TJP, carotid body tumor and vestibular schwannoma. D. mIHC of the pathological sections of characteristic genes of fibroblasts subtypes. (Scale bar:100 μm) E. Mcode network postulated by cytoscape in myofibroblasts and bone remodeling related fibroblasts based on the differential expressed genes.

and *MYLK*.

Previous studies used various marker gene sets to evaluate these subclusters [27]. Enrichment analysis across the six main fibroblast subgroups revealed functional diversity, with angiogenesis (GO: 0001525) as the common thread. However, significant heterogeneity was evident in the gene expression profiles and associated biological pathways. Fib_0 was associated with extracellular matrix organization (GO: 0030198) and external encapsulating structure organization (GO: 0045229), whereas Fib_1 was distinguished by immediate early genes such as *HSPA1A*, *HSPB1*, *EGR1*, *FOS*, and *JUN*, which are involved in the response to unfolded proteins (GO: 0006986) and topologically incorrect proteins (GO: 00035966), suggesting that Fib_1 plays crucial roles in the stress response. Fib_2 was highly expressed in *MYH11* and enriched in muscle contraction (GO: 0006936) and muscle system processes (GO: 0003012). Fib_3 showed low expression of *PDGFRB* and high expression of extracellular matrix signatures, including *COL5A1*, *COL6A3*, *POSTN*, *LUM*, *DCN*, and *FAP*, which were enriched in response to oxygen levels (GO: 0070482), extracellular matrix organization (GO: 0030198), extracellular structure organization (GO: 0043062), and external encapsulating structure organization (GO: 0045229). Fib_4 was enriched in response to peptides (GO: 1901652), ameboidal-type cell migration (GO: 0001667), and connective tissue development (GO: 0061448), and Fib_5 was highly expressed in *CCL2* and *THBS1*, and scored highly in the following GO terms: regulation of epithelial cell apoptotic process (GO: 1904035) and endothelial cell apoptotic process (GO: 0072577) (Supplemental Figs. S3A and S3B).

Notably, Fib_0, Fib_1, Fib_2, Fib_4, and Fib_5 expressed vascular-related gene sets [41] and scored highly in the GO term angiogenesis involved in wound healing (GO: 0060055). Fib_3 scored highly in ossification (GO: 0001503), osteoblast differentiation (GO: 0001649), multicellular organism signaling (GO: 0035637), and multicellular organism process (GO: 0044706), similar to a fibroblast subcluster found in cholesteatomas [42] (Fig. 2B).

To compare fibroblast features in TJPs with tumors in similar locations, scRNA-seq datasets of vestibular schwannomas (VSs) [43] and carotid body tumors (CBTs) [8] were analyzed, and the fibroblast data were separated from these datasets. Following batch correction and similar processing, all fibroblast datasets were merged. Fibroblasts from VSs showed characteristics similar to those of

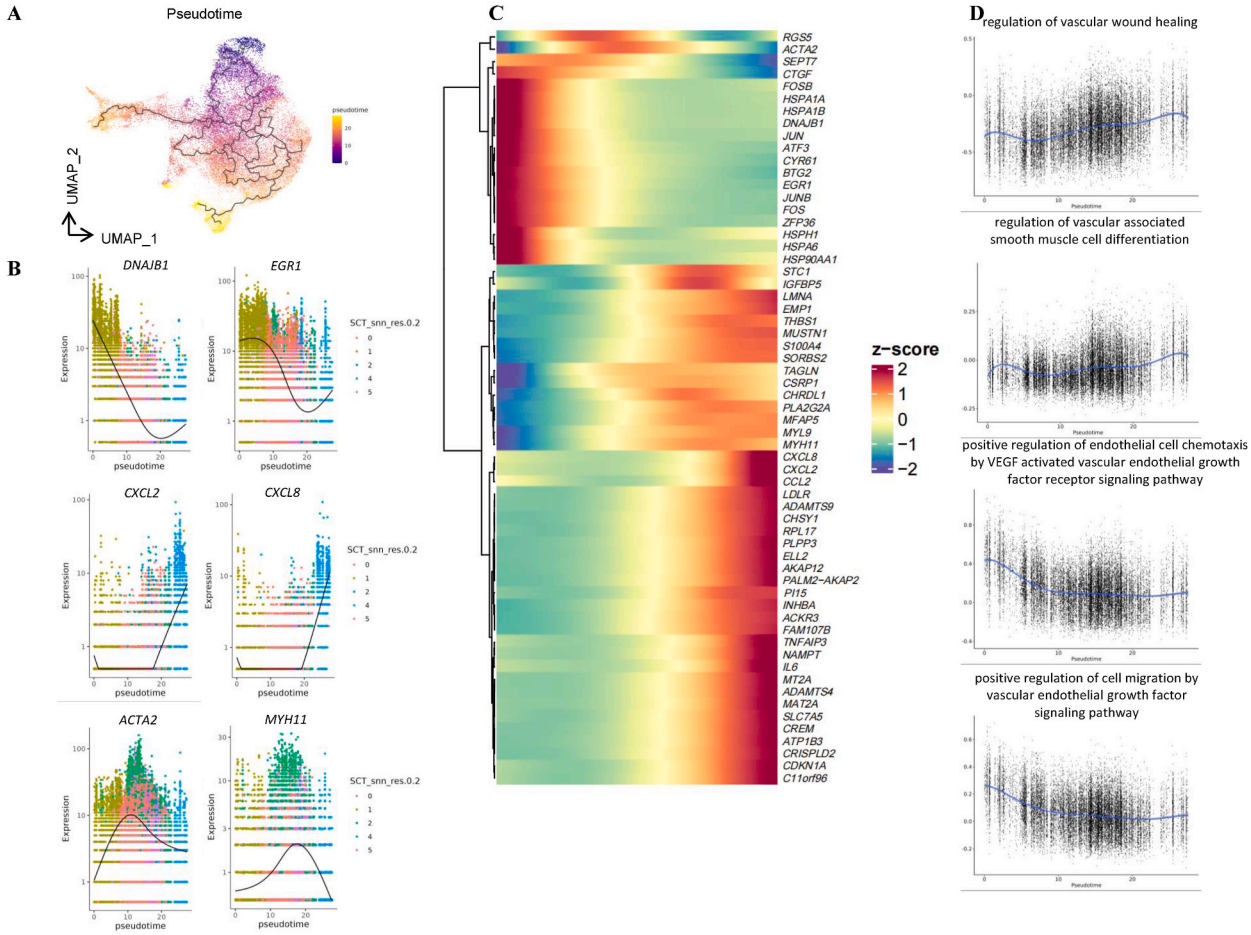

Fig. 3. Pseudotime trajectory postulated in fibroblasts A. Pseudotime postulated by monocle3 showing the dynamics within the angiogenesis related fibroblasts. B. Jitter plots depicting the change of selected genes. C. Heatmap of the genes with significant expression change along the pseudotime. D. Changing of selected enrichment terms with the progression of pseudotime.

Fib_3 and Fib_5, whereas fibroblasts from CBTs resembled those of Fib_0, Fib_2, and Fib_4, although with distinct differences (Fig. 2C). mIHC staining confirmed the presence of primary fibroblast subsets (*TAGLN*, *APOD*, and *MYH11*) in the TJP samples (Fig. 2D).

The protein–protein interactions were postulated using the STRING database (https://string-db.org/) and subsequently analyzed using Mcode revealed a distinct subnetwork within the differentially expressed genes of each group (Fig. 2E). The network within myofibroblasts featured genes including *KCNJ8* and *ABCC9* (implicated in vascular smooth muscle development) as well as *HIF1α* (a key regulator of angiogenesis frequently activated in tumors or angiogenesis-related fibroblasts). Constitutive activation of *HIF1* is frequently observed in human tumors as a major regulator of angiogenesis [44]. Another notable network encompassed *NGF* and *AXL*, both known to play roles in PC12 cell differentiation [45]. Bone remodeling-associated fibroblasts revealed networks involving genes such as *BGN, CTSK*, and *SPP1*, which are central to bone resorption and calcification [46].

3.3. Pseudotime trajectory of fibroblasts in TJPs

Because fibroblasts in TJPs showed heterogeneity, we used pseudotime trajectory analysis to further investigate the possible gradual differentiation and maturation of these cells. Fibroblasts were delineated into two primary trajectories, corresponding to myofibroblasts and bone remodeling-related fibroblasts, respectively (Fig. 3A). The trajectories of myofibroblasts were more intricate and well-defined than those observed in their bone-remodeling counterparts.

The cell cycle compositions of different fibroblast clusters were analyzed using cell cycle gene sets and scored using the Seurat function (Supplemental Fig. S4B). After combining the results of enrichment analysis and cell cycle scoring, two distinct routes originating from the Fib_1 cluster and directed towards Fib_0, Fib_2, Fib_4, and Fib_5 were observed. Throughout the pseudotime, the expression of characteristic genes such as *DNAJB1* and *EGR1* was initially prominent, followed by upregulation of *MYH11* and *ACTA2* in the middle stages and *CXCL2* and *CXCL8* in the later stages (Fig. 3B and C).

Enrichment and pseudotime analyses were integrated to gain a better understanding of functional changes. The progression of

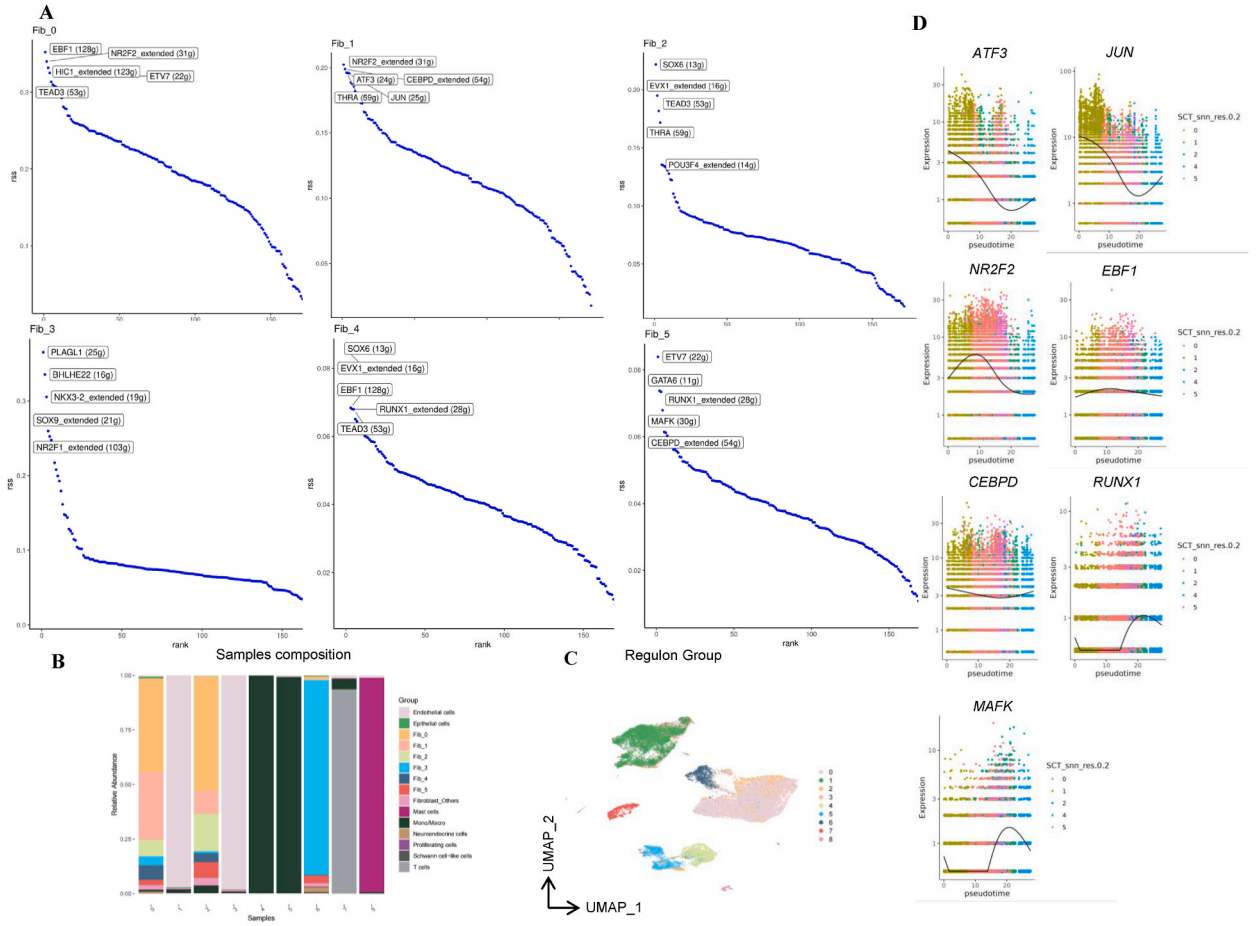

Fig. 4. Regulatory network in TJP A. Regulon enrichment score for fibroblasts subcluster 0–5 based on SCENIC calculation with top regulon labeled. B. Stack bar chart of the relative composition of cell types in the groups based on transcription activity. C. Umap plot of groups based on transcription factor activity. D. Transcription factor expression that changes along the pseudotime.

myofibroblasts through pseudotime was marked by increases in the scores for the GO terms regulation of vascular wound healing (GO: 0061043) and regulation of vascular-associated smooth muscle cell differentiation (GO: 1905063). The scores of the following GO terms showed an initial decrease: positive regulation of endothelial cell chemotaxis by the vascular endothelial growth factor (VEGF) activated receptor signaling pathway (GO: 0038033) and positive regulation of cell migration by the VEGF signaling pathway (GO: 0038089). These patterns suggest that myofibroblast functionality gradually transforms along its pseudotime trajectory, indicating its evolving roles within the tumor microenvironment (Fig. 3D).

3.4. Transcriptional network analysis of fibroblasts

TFs are proteins that influence various cellular processes and responses by regulating RNA synthesis [47]. Previous studies highlighted the roles of various TFs in angiogenesis and the HNPGL microenvironment [48–51]. Using scRNA-seq, the regulatory activity of specific TFs can be postulated using bioinformatics tools, such as SCENIC. We performed this analysis on the scRNA-seq data, focusing on fibroblasts, to provide additional perspective in addition to examining expression levels.

Regulons with high fibroblast activity included *EBF1*, *TEAD3*, *HIC1, CEBPD*, and *NR2F2*. Further analysis of fibroblast clustering revealed distinct patterns of regulatory activity, which were particularly high among different fibroblast subgroups. Within the Fib_3 cluster, TFs such as *PLAGL1*, *BHLHE22*, *NKX3-2*, *SOX9*, and *NR2F1* showed the highest transcriptional regulatory activity. In contrast, the leading representative TFs in the regulatory network were *EBF1*, *NR2F2*, *HIC1*, *TEAD3*, and *ETV7* in Fib_0; *NR2F2*, *ATF3*, *THRA*, *CEBPD*, and *JUN* in Fib_1; *SOX6*, *EVX1*, *TEAD3*, *THRA*, and *POU3F4* in Fib_2; *SOX6*, *EVX1*, *EBF1*, *TEAD3*, and *RUNX1* in Fib_4; and *ETV7*, *GATA6*, *RUNX1*, *MAFK*, and *CEBPD* in Fib_5 (Fig. 4A, Supplemental Figs. S5A and S5B). Analysis of the cluster based on regulon activity and differentially expressed genes revealed that the transcriptional regulatory pattern exhibited by Fib_3 differed from that of the other fibroblasts (Fig. 4B and C). This result was supported by the high activity of *GATA6*, *CREB3L1*, *RUNX2*, *MEIS1*, *PLAGL1*,

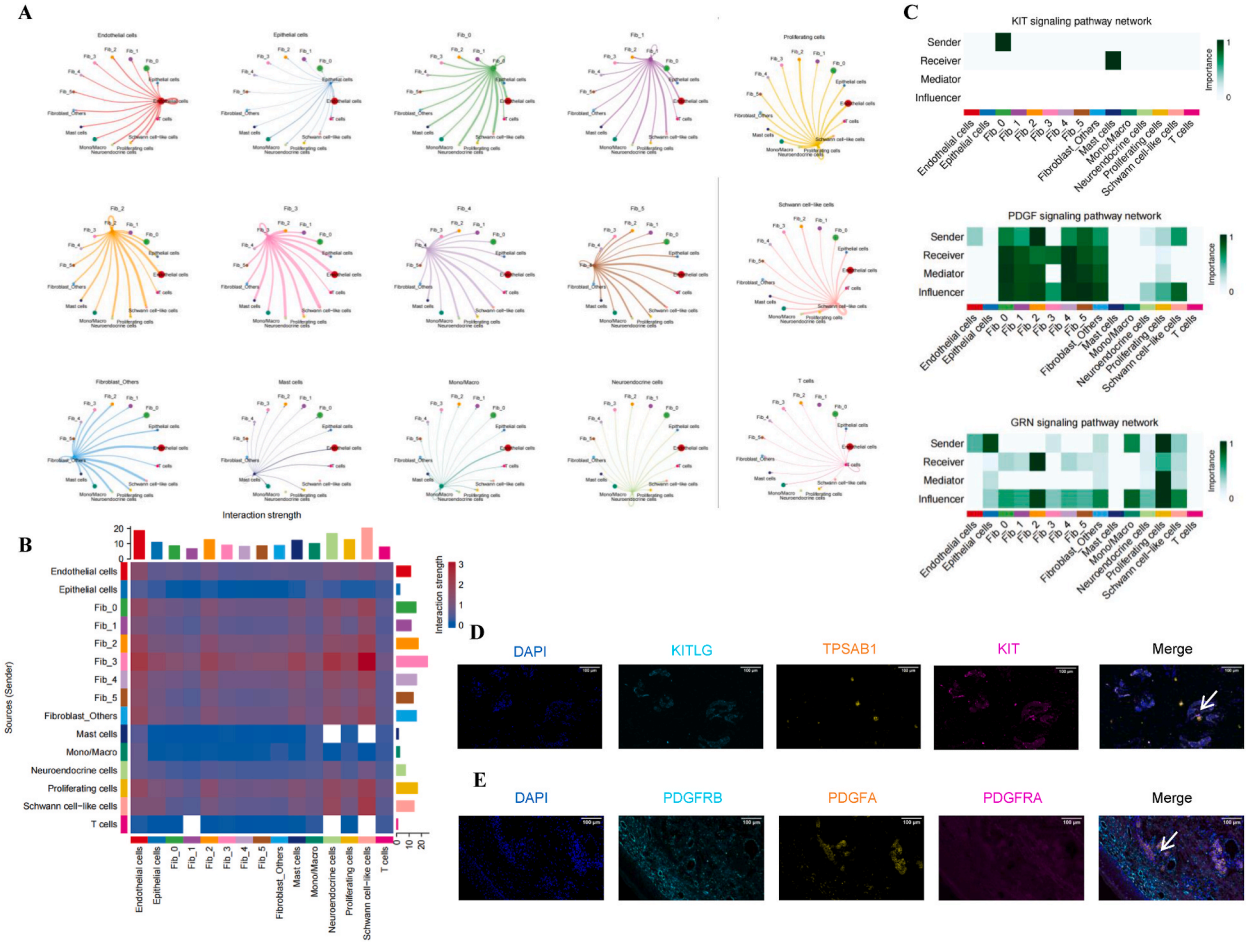

Fig. 5. Cell-cell communication in TJP A. Circular plot of the overall cell-cell communication for each cell type. B. Heatmap showing the interaction strength between different cell types. C. Topological network visualization of KIT, GRN and PDGF signaling pathway between different cell types. D. mIHC of DAPI and different cell-cell communication participants on TJP pathological sections. Arrow pointed to the selected contact cells. (Scale bar: 100 μm).

BHLHE22, and *TWIST1* in Fib_3, despite sharing some common TFs such as *FOXO3* and *ELK1* with other clusters (Supplemental Fig. S5C).

To further explore changes in regulatory activity along the pseudotime trajectory, the top regulons in myofibroblasts were analyzed. Notably, only *MAFK*, *RUNX1*, *CEBPD*, *ATF3*, *EBF1*, *JUN*, and *NR2F2* exhibited changes in expression along this trajectory, indicating that differences in transcriptional regulatory activity may not always correspond to changes in transcriptomic expression levels (Fig. 4D).

3.5. Diverse intercellular networks observed in TJPs

Cell–cell communication is the process by which cells exchange biochemical and physical signals that influence their phenotype and function [52]. This process can be depicted in detail using scRNA-seq data and bioinformatics tools [53].

Previous studies showed that tumorigenesis is closely related to cell–cell interactions within the microenvironment [54]. To further explore these interactions among different cell types and identify features of the microenvironment, cell–cell communication analysis was performed using TJP scRNA-seq data. Multiple cell–cell interaction pathways were observed in TJPs (Supplemental Fig. S6A). Fibroblasts emerged as central communicators, displaying the most extensive interaction strength with other cell types, underscoring their key roles in the microenvironment (Fig. 5A and B). Among the cell communication pathways, topological analysis revealed that the KIT, progranulin (GRN), and platelet-derived growth factor (PDGF) signaling pathways differed between fibroblast subpopulations (Fig. 5C). In the KIT signaling network, Fib_0 showed a unique connection with mast cells. In the GRN signaling network, Fib_2 displayed a unique connection with proliferating cells, neuroendocrine cells, Schwann cell-like cells, and epithelial cells. In the PDGF signaling network, fibroblasts exhibited strong interactions with endothelial and proliferating cells, neuroendocrine cells, and Schwann cell-like cells. To verify the hypothesized cell–cell interactions, mIHC was performed. In the TJP sections, KIT and KIT ligand (KITLG) were specifically expressed in proximity, with KITLG observed in mast cells, indicating the existence of a KIT–KITLG pathway between fibroblasts and mast cells (Fig. 5D). Cells expressing PDGF subunit A were in contact with the cells expressing PDGF receptor alpha (PDGFRA) and PDGF receptor beta (PDGFRB) (Fig. 5E). However, direct contact was not observed in the GRN pathway, likely because of the relatively low percentage of neuroendocrine cells in TJPs (Supplemental Fig. S6B).

To compare the differences in TJP cellular communication between the recurrent and primary groups, we again performed CellChat from the differences in overall information flow between 1 recurrent and 5 primary regrowth samples, we found that the signaling pathways that were highly enriched in recurrent TJPs compared to the primary samples were IL6, GALECTIN, TGFb, CSF3, BMP, CHEMERIN, ANGPTL, TRAIL, MIF, SEMA3, GAS, PTN, CXCL, GRN, PDGF, EGF, VISFATIN, and ANGPT pathways (Fig. 6A). To

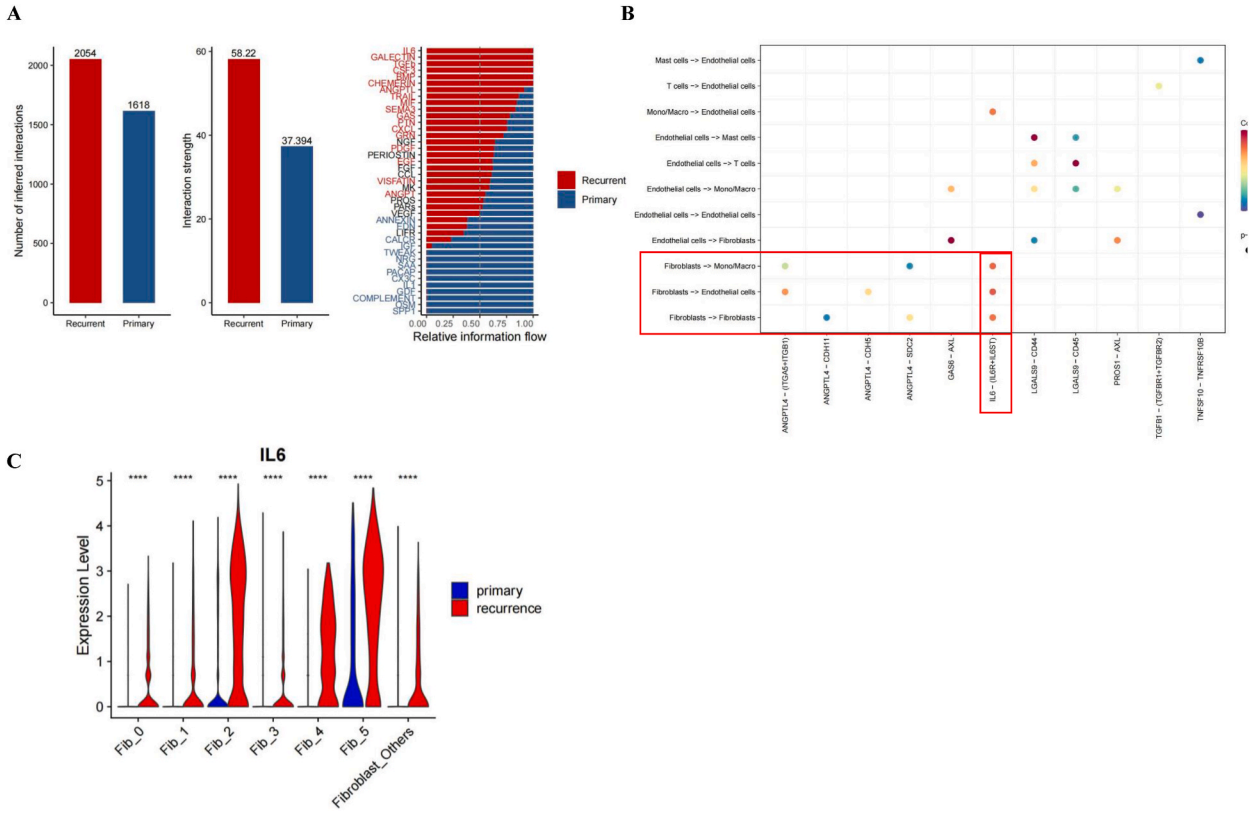

Fig. 6. Comparision of cell-cell communication between the recurrent and primary groups.

understand the ligand-receptor interactions of these pathways among cell populations in the relapse group, we demonstrated the probability of pathway-regulated communication among cell populations (Fig. 6B), with a high probability of the paired pathway IL6-(IL6R + IL6ST) and in which fibroblast-originated IL6 interacts with endothelial cells, macrophages, etc. through IL6-(IL6R + IL6ST) interactions. We found that IL6 expression was also significantly higher in fibroblasts in the recurrent group than in the primary group, and was significantly higher mainly in the myofibroblasts Fib_2, Fib_4, and Fib_5 (Fig. 6C). We speculated that IL6+ fibroblasts might be involved in the tumor recurrence process of TJP through the IL6 pathway.

A Key pathways were identified by contrasting the overall information flow within the network of the Recurrent and Primary groups. Pathways highlighted in black font signify equal importance, while those in other colors denote enrichment specific to each group. **B** All the significant ligand-receptor pairs that contribute to the signaling sending from recurrent groups. Deeper shades of red indicate higher communication probabilities, with receptor communication probabilities in the chart being significant at $p < 0.01$. **C** Expression of IL6 in different subpopulations of fibroblasts in the recurrent and primary groups. ($p < 0.0001$).

4. Discussion

Most studies of TJP focused on its clinical presentation and genetic characteristics [55]. Although these studies provided important insights into the disease, further investigation of the transcriptomic characteristics of TJP, particularly in comparison with those of other HNPGLs, is needed to understand the clinical differences, including the progression or development of new central nerve deficits [55]. In the current study, scRNA-seq was used as the primary approach to examine the transcriptomic landscape of TJP, along with whole-exome sequencing. This investigation revealed the heterogeneity of fibroblasts, improving our understanding of their role in the TJP microenvironment.

In terms of cellular components, the main cell types in TJPs were consistent with those determined in previous studies of PGLs [8,56]. Interestingly, fibroblasts were the most abundant, whereas neuroendocrine cells were less prevalent, a distribution reflecting that of benign ganglioneuromas [40] and providing insights into the asymptomatic nature of some PGLs [57]. The prominence of immature smooth muscle cell markers (*TAGLN*) over mature markers (*ACTA2* and *MYH11*) in Fib_0 and Fib_1 supports the clinical challenge of hemostasis despite an ample blood supply. Mitochondrial reads (25 %) showed a high fraction of samples, indicating cell death induced by preoperative protective stenting of the internal carotid artery [58]. This effect may result in a biased reconstruction of the relationships between various cellular subsets. The average ratio of ACTA2-positive cells in pathological sections was approximately 32 %, which is lower than that obtained using sequencing data in the current study, likely because of the heterogeneity inherent to TJP.

Although typically considered tumors, some PGLs exhibit slow growth and indolent characteristics, indicating heterogeneity within these tumors [59]. Previous studies described the roles of fibroblasts in various tumors, including their involvement in reconstructing the extracellular matrix, contributing to immunosuppression, and promoting angiogenesis. In the context of PGLs, *in vitro* studies focused on the mechanisms of fibroblasts, including the ERK1/2 and integrin pathways, as well as fibroblast clustering using single-cell nuclei sequencing [38,60,61]. However, TJP fibroblasts have not been examined using scRNA-seq. To the best of our knowledge, this is the first study to recluster fibroblasts in TJPs, revealing significant heterogeneity.

Based on differentially expressed genes, fibroblasts in TJP can be divided into two main groups, myofibroblasts and bone remodeling-associated fibroblasts. Bone remodeling-associated fibroblasts were similar to those in VSs [43] and myofibroblasts were similar to those in CBTs [8]. This finding indicates that the unique characteristics of fibroblasts in TJPs may contribute partially to the clinical distinctions observed between PGLs and lateral skull base tumors.

Compared with bone remodeling-associated fibroblasts, myofibroblasts exhibited more complex pseudotime trajectories and significant expression transitions, such as high expression of immediate early genes in the early stage and *ACTA2*, *MYH11*, *CXCL2*, and *CXCL8* in the late stage. However, the cause of immediate early gene activation can be attributed to several factors, such as biological phenomena occurring within the tissue or surgical excision [62]. *HSF1* is frequently activated in cancer-associated fibroblasts, which are potent enablers of malignancy.

Fibroblasts displayed distinct TF activity patterns. High-activity TFs in fibroblasts, such as *TWIST1* have been linked to tumor growth in neuroblastomas. *TEAD3* inhibits proliferation in prostate cancer [63], and *NR2F2* functions as a central regulator of tumor angiogenesis and lymphangiogenesis by regulating *VEGF/VEGFR*, *Ang-1/Tie2*, and other pathways involved in manipulation of the tumor microenvironment [64]. *EBF1* fibroblasts influence early lung development and fibrotic conditions [65]. *CEBPD* is the main TF for hypoxia regulatory proteins in glioblastoma, enhancing hypoxia-induced tumor invasion. Notably, the heightened activity of the *CREB* family aligns with the metabolic activity of pancreatic ductal adenocarcinoma fibroblasts, which is pertinent to prognosis and immunotherapy responses [66]. Within the pancreatic ductal adenocarcinomas, *FOXO3* can induce stem cell properties, and its depletion leads to fibroblast phenotypic changes in pulmonary fibrosis, thereby enhancing the proliferation and differentiation of myofibroblasts. Finally, the association between *NR2F1* and tumor dormancy in breast cancer emphasizes the importance of inflammatory fibroblasts in cancer progression.

In addition to revealing transcriptomic features, the regulatory network highlights the heterogeneity of fibroblasts and their potential pro-tumor and angiogenic roles in TJP. The activity of TFs and their target genes also differed between the two main fibroblast subtypes.

The interactions of fibroblasts with other cell types were also evaluated in TJP. Fibroblasts exhibited the strongest interaction with other cell types, underscoring their critical role in the microenvironment. Among the observed communication patterns, some have not been previously reported for HNPGLs. For instance, in the KIT cell–cell communication pathway, interactions between Fib_0 and mast cells were noted in the urethral structure and identified as potential targets for tissue fibrosis [67]. Additionally, suppression of KITLG inhibits proliferation, invasion, and metastasis in nasopharyngeal cancer. Enrichment of the PDGF pathway between endothelial cells

and fibroblasts suggests that endothelial cell interactions are involved in tumor microenvironment fibrosis [68,69]. Although the KIT and PDGF pathways were confirmed, enrichment of the GRN pathway was not observed, likely because of the relatively low percentage of neuroendocrine cells in TJPs.

The IL6 signaling pathway was found to be significantly enriched in the recurrent group, and IL6 expression was also significantly higher in fibroblasts in the recurrent group than in the primary group, mainly in myofibroblasts, which interacted with endothelial cells and macrophages via IL6- (IL6R + IL6ST). High levels of M2-type macrophages and Tregs have been reported to correlate between poorer prognosis in PGL [70]. Vocal cord leukoplakia fibroblasts have been reported to produce immunosuppression through secretion of IL6, and significant reversal of precancerous lesion progression by blocking IL-6R has been demonstrated in a mouse model [71]. IL6 expression was found to be an independent prognostic factor in esophageal cancer, and it was experimentally demonstrated that IL6 increased HIF-1α expression and induced immunosuppression by competing with immune cells for glucose through enhanced glucose uptake by cancer cells [72]. We hypothesized that high expression of IL6 by recurrent constitutive fibroblasts could regulate the immune microenvironment of the tumor, which may be one of the reasons for tumor recurrence and regrowth, however, this also needs further experimental verification.

These findings present a landscape of TJPs encompassing transcriptomic, regulatory network, and cell–cell communication features and highlight the essential role and heterogeneity of fibroblasts in the microenvironment. These findings should be interpreted with caution, as normal tissue from the lateral skull base or paraganglia could not be obtained to serve as controls because of surgical indications and limitations. As the current results are based on clinical samples and experiments, further studies using appropriate *in vitro* or animal models are necessary to validate these observations and determine the underlying mechanisms of fibroblast involvement in TJPs.

5. Conclusion

In conclusion, scRNA-seq analysis provides a comprehensive perspective on the HNPGL microenvironment, highlighting the role of fibroblasts in pathological processes. Fibroblasts exhibit heterogeneity in terms of transcriptomics, regulatory networks, cell–cell communication, and pseudotime characteristics. Fibroblasts in TJPs can be further classified into myofibroblasts, akin to those in CBTs, and bone remodeling-associated fibroblasts, resembling those in VSs. Fibroblasts strongly interact with mast and endothelial cells through pathways such as KIT, which have not been widely reported. IL6 signaling pathway of fibroblasts interacting with macrophages and endothelial cells is significantly enriched in recurrent TJP. These results offer a multilevel atlas of HNPGL, providing insights into fibroblasts and a foundation for understanding their development and clinical features.

Ethics statement

This study was approved by The Shanghai Sixth People's Hospital Institutional Ethics Review Board (approval No. 2021-242-1). Written informed consent was obtained from all the participants.

Data availability

scRNA-seq data were deposited in https://www.biosino.org/node/project/detail/OEP004177 and WES data were deposited in https://www.biosino.org/node/project/detail/OEP004193. The data supporting of this study are available from the corresponding author on reasonable request.

CRediT authorship contribution statement

Shengming Wang: Conceptualization, Data curation, Formal analysis, Methodology, Software, Writing – original draft, Writing – review & editing. **Boya Zhang:** Formal analysis, Investigation, Methodology, Writing – review & editing. **Zihan Lou:** Formal analysis, Methodology. **Yibing Hu:** Data curation, Formal analysis. **Jian Wang:** Conceptualization, Writing – review & editing. **Jingjing Wang:** Funding acquisition, Resources, Supervision, Validation. **Zhengnong Chen:** Conceptualization, Funding acquisition, Resources, Supervision, Visualization. **Shankai Yin:** Conceptualization, Supervision, Validation, Visualization, Writing – review & editing.

Declaration of competing interest

The authors declare that they have no known competing financial interests or personal relationships that could have appeared to influence the work reported in this paper.

Acknowledgement

This research was supported by the National Natural Science Foundation of China (No. 82071040), and Science and Technology Innovation Plan of Shanghai Science and Technology Commission (No. 22YF1432700).

Appendix A. Supplementary data

Supplementary data to this article can be found online at https://doi.org/10.1016/j.heliyon.2024.e35478.

References

[1] N. Aygun, M. Uludag, Pheochromocytoma and paraganglioma: from epidemiology to clinical findings, Sisli Etfal Hastan Tip Bul 54 (2) (2020) 159–168.
[2] S.M.J. Fliedner, et al., Pheochromocytoma and paraganglioma: genotype versus anatomic location as determinants of tumor phenotype, Cell Tissue Res. 372 (2) (2018) 347–365.
[3] L. Sandow, et al., Paraganglioma of the head and neck: a review, Endocr. Pract. 29 (2) (2023) 141–147.
[4] M.D. Williams, Paragangliomas of the head and neck: an overview from diagnosis to genetics, Head Neck Pathol 11 (3) (2017) 278–287.
[5] P.C. Weber, S. Patel, Jugulotympanic paragangliomas, Otolaryngol. Clin. 34 (6) (2001) 1231–1240, x.
[6] C. Valero, et al., Head and neck paragangliomas: 30-year experience, Head Neck 42 (9) (2020) 2486–2495.
[7] N. Kuroda, et al., Possible identification of third stromal component in extraadrenal paraganglioma: myofibroblast in fibrous band and capsule, Med. Mol. Morphol. 41 (1) (2008) 59–61.
[8] M. Zethoven, et al., Single-nuclei and bulk-tissue gene-expression analysis of pheochromocytoma and paraganglioma links disease subtypes with tumor microenvironment, Nat. Commun. 13 (1) (2022) 6262.
[9] V. D'Antongiovanni, et al., The microenvironment induces collective migration in SDHB-silenced mouse pheochromocytoma spheroids, Endocr. Relat. Cancer 24 (10) (2017) 555–564.
[10] P.D.P. Böck, Handbuch der mikroskopischen Anatomie des Menschen, 1982.
[11] S. Martinelli, et al., Tumour microenvironment in pheochromocytoma and paraganglioma, Front. Endocrinol. 14 (2023) 1137456.
[12] X. Gao, et al., Histopathological analysis of tumor microenvironment and angiogenesis in pheochromocytoma, Front. Endocrinol. 11 (2020) 587779.
[13] J. Fischer, T. Ayers, Single nucleus RNA-sequencing: how it's done, applications and limitations, Emerging Topics in Life Sciences 5 (5) (2021) 687–690.
[14] H.C. Fan, et al., Expression profiling. Combinatorial labeling of single cells for gene expression cytometry, Science 347 (6222) (2015) 1258367.
[15] I. Korsunsky, et al., Fast, sensitive and accurate integration of single-cell data with Harmony, Nat. Methods 16 (12) (2019) 1289–1296.
[16] D. Aran, et al., Reference-based analysis of lung single-cell sequencing reveals a transitional profibrotic macrophage, Nat. Immunol. 20 (2) (2019) 163–172.
[17] N.A. Mabbott, et al., An expression atlas of human primary cells: inference of gene function from coexpression networks, BMC Genom. 14 (2013) 632.
[18] T. Wu, et al., clusterProfiler 4.0: a universal enrichment tool for interpreting omics data, Innovation 2 (3) (2021) 100141.
[19] C. Trapnell, et al., The dynamics and regulators of cell fate decisions are revealed by pseudotemporal ordering of single cells, Nat. Biotechnol. 32 (4) (2014) 381–386.
[20] S. Aibar, et al., SCENIC: single-cell regulatory network inference and clustering, Nat. Methods 14 (11) (2017) 1083–1086.
[21] V.A. Huynh-Thu, et al., Inferring regulatory networks from expression data using tree-based methods, PLoS One 5 (9) (2010).
[22] H. Li, R. Durbin, Fast and accurate short read alignment with Burrows-Wheeler transform, Bioinformatics 25 (14) (2009) 1754–1760.
[23] H. Li, et al., The sequence alignment/map format and SAMtools, Bioinformatics 25 (16) (2009) 2078–2079.
[24] P. Bankhead, et al., QuPath: open source software for digital pathology image analysis, Sci. Rep. 7 (1) (2017) 16878.
[25] A. Butler, et al., Integrating single-cell transcriptomic data across different conditions, technologies, and species, Nat. Biotechnol. 36 (5) (2018) 411–420.
[26] P. Brazda, et al., Extensive patient-to-patient single nucleus transcriptome heterogeneity in pheochromocytomas and paragangliomas, Front. Oncol. 12 (2022) 965168.
[27] Z. Chen, et al., Single-cell RNA sequencing highlights the role of inflammatory cancer-associated fibroblasts in bladder urothelial carcinoma, Nat. Commun. 11 (1) (2020) 5077.
[28] J. Qian, et al., A pan-cancer blueprint of the heterogeneous tumor microenvironment revealed by single-cell profiling, Cell Res. 30 (9) (2020) 745–762.
[29] J.L. Bautista, et al., Single-cell transcriptional profiling of human thymic stroma uncovers novel cellular heterogeneity in the thymic medulla, Nat. Commun. 12 (1) (2021) 1096.
[30] L. Communal, et al., A keratin 7 and E-cadherin signature is highly predictive of tubo-ovarian high-grade serous carcinoma prognosis, Int. J. Mol. Sci. 22 (10) (2021).
[31] P. Kameneva, et al., Single-cell transcriptomics of human embryos identifies multiple sympathoblast lineages with potential implications for neuroblastoma origin, Nat. Genet. 53 (5) (2021) 694–706.
[32] A. Furlan, I. Adameyko, Schwann cell precursor: a neural crest cell in disguise? Dev. Biol. 444 (Suppl 1) (2018) S25–S35.
[33] W. Zhao, et al., Deconvolution of cell type-specific drug responses in human tumor tissue with single-cell RNA-seq, Genome Med. 13 (1) (2021) 82.
[34] A. Sebastian, et al., Single-cell RNA-Seq reveals changes in immune landscape in post-traumatic osteoarthritis, Front. Immunol. 13 (2022) 938075.
[35] P. van Galen, et al., Single-cell RNA-Seq reveals AML hierarchies relevant to disease progression and immunity, Cell 176 (6) (2019), 1265-81.e24.
[36] Morgenstern N. Ben-Baruch, et al., Single-cell RNA sequencing of mast cells in eosinophilic esophagitis reveals heterogeneity, local proliferation, and activation that persists in remission, J. Allergy Clin. Immunol. 149 (6) (2022) 2062–2077.
[37] N.A. Winter, et al., Sputum mast cell/basophil gene expression relates to inflammatory and clinical features of severe asthma, J. Allergy Clin. Immunol. 148 (2) (2021) 428–438.
[38] S.V. Puram, et al., Single-cell transcriptomic analysis of primary and metastatic tumor ecosystems in head and neck cancer, Cell 171 (7) (2017), 1611-24.e24.
[39] O.C. Bedoya-Reina, et al., Single-nuclei transcriptomes from human adrenal gland reveal distinct cellular identities of low and high-risk neuroblastoma tumors, Nat. Commun. 12 (1) (2021) 5309.
[40] Q. Liu, et al., Single-cell landscape analysis reveals distinct regression trajectories and novel prognostic biomarkers in primary neuroblastoma, Genes Dis 9 (6) (2022) 1624–1638.
[41] C. Wu, et al., Single-cell characterization of malignant phenotypes and microenvironment alteration in retinoblastoma, Cell Death Dis. 13 (5) (2022) 438.
[42] K. Shimizu, et al., Single-cell transcriptomics of human cholesteatoma identifies an activin A-producing osteoclastogenic fibroblast subset inducing bone destruction, Nat. Commun. 14 (1) (2023) 4417.
[43] M. Xu, et al., Single-cell RNA-Seq reveals heterogeneity of cell communications between Schwann cells and fibroblasts within vestibular schwannoma microenvironment, Am. J. Pathol. 192 (9) (2022) 1230–1249.
[44] A.L. Casillas, et al., Direct phosphorylation and stabilization of HIF-1α by PIM1 kinase drives angiogenesis in solid tumors, Oncogene 40 (32) (2021) 5142–5152.
[45] Q. Wang, et al., Expressions of Axl and Tyro-3 receptors are under regulation of nerve growth factor and are involved in differentiation of PC12 cells, Neurosci. Bull. 27 (1) (2011) 15–22.
[46] L.G.M. Heezen, et al., Spatial transcriptomics reveal markers of histopathological changes in Duchenne muscular dystrophy mouse models, Nat. Commun. 14 (1) (2023) 4909.
[47] P. Weidemüller, et al., Transcription factors: bridge between cell signaling and gene regulation, Proteomics 21 (23–24) (2021) e2000034.
[48] Y. Mao, et al., Fibroblasts mediate the angiogenesis of pheochromocytoma by increasing COX4I2 expression, Front. Oncol. 12 (2022) 938123.
[49] J. Favier, et al., Rationale for anti-angiogenic therapy in pheochromocytoma and paraganglioma, Endocr. Pathol. 23 (1) (2012) 34–42.
[50] F. Verginelli, et al., Paragangliomas arise through an autonomous vasculo-angio-neurogenic program inhibited by imatinib, Acta Neuropathol. 135 (5) (2018) 779–798.

[51] A. Guha, et al., A systematic review on the genetic analysis of paragangliomas: primarily focused on head and neck paragangliomas, Neoplasma 66 (5) (2019) 671–680.
[52] A.A. Almet, et al., The landscape of cell-cell communication through single-cell transcriptomics, Curr. Opin. Struct. Biol. 26 (2021) 12–23.
[53] A.J. Wilk, et al., Comparative analysis of cell-cell communication at single-cell resolution, Nat. Biotechnol. (2023).
[54] P. Li, et al., Epigenetic silencing of microRNA-149 in cancer-associated fibroblasts mediates prostaglandin E2/interleukin-6 signaling in the tumor microenvironment, Cell Res. 25 (5) (2015) 588–603.
[55] J.A. Forbes, et al., Jugulotympanic paragangliomas: 75 years of evolution in understanding, Neurosurg. Focus 33 (2) (2012) E13.
[56] O. Mete, et al., Overview of the 2022 WHO classification of paragangliomas and pheochromocytomas, Endocr. Pathol. 33 (1) (2022) 90–114.
[57] G. Constantinescu, et al., Silent pheochromocytoma and paraganglioma: systematic review and proposed definitions for standardized terminology, Front. Endocrinol. 13 (2022) 1021420.
[58] P. Pigny, et al., Paraganglioma after maternal transmission of a succinate dehydrogenase gene mutation, J. Clin. Endocrinol. Metab. 93 (5) (2008) 1609–1615.
[59] E.F. Cleere, et al., Contemporary management of paragangliomas of the head and neck, Laryngoscope Investig Otolaryngol 7 (1) (2022) 93–107.
[60] C.J. Wei, et al., A narrative review of the role of fibroblasts in the growth and development of neurogenic tumors, Ann. Transl. Med. 8 (21) (2020) 1462.
[61] A. Martin, et al., Fibroblast deficiency of insulin-like growth factor 1 receptor type 1 (IGF1R) impairs initial steps of murine pheochromocytoma development, Biochimie 163 (2019) 108–116.
[62] A.Z. Wang, et al., Single-cell profiling of human dura and meningioma reveals cellular meningeal landscape and insights into meningioma immune response, Genome Med. 14 (1) (2022) 49.
[63] C. Wang, et al., TEAD3 inhibits the proliferation and metastasis of prostate cancer via suppressing ADRBK2, Biochem. Biophys. Res. Commun. 654 (2023) 120–127.
[64] M. Xu, et al., The role of the orphan nuclear receptor COUP-TFII in tumorigenesis, Acta Pharmacol. Sin. 36 (1) (2015) 32–36.
[65] X. Liu, et al., Multiple fibroblast subtypes contribute to matrix deposition in pulmonary fibrosis, Am. J. Respir. Cell Mol. Biol. 69 (1) (2023) 45–56.
[66] Y. Wang, et al., Single-cell analysis of pancreatic ductal adenocarcinoma identifies a novel fibroblast subtype associated with poor prognosis but better immunotherapy response, Cell Discov 7 (1) (2021) 36.
[67] K. Li, et al., Single-cell transcriptome reveals cellular heterogeneity and lineage-specific regulatory changes of fibroblasts in post-traumatic urethral stricture, Biochem Biophys Rep 33 (2023) 101431.
[68] X. Ren, et al., PDGF-BB regulates the transformation of fibroblasts into cancer-associated fibroblasts via the lncRNA LURAP1L-AS1/LURAP1L/IKK/IκB/NF-κB signaling pathway, Oncol. Lett. 22 (1) (2021) 537.
[69] P. Juhl, et al., Dermal fibroblasts have different extracellular matrix profiles induced by TGF-β, PDGF and IL-6 in a model for skin fibrosis, Sci. Rep. 10 (1) (2020) 17300.
[70] B. Calsina, et al., Genomic and immune landscape of metastatic pheochromocytoma and paraganglioma, Nat. Commun. 14 (1) (2023) 1122.
[71] Y. Fang, et al., Cancer-associated fibroblast-like fibroblasts in vocal fold leukoplakia suppress CD8(+)T cell functions by inducing IL-6 autocrine loop and interacting with Th17 cells, Cancer Lett. 546 (2022) 215839.
[72] N. Nishiwaki, et al., Overcoming cancer-associated fibroblast-induced immunosuppression by anti-interleukin-6 receptor antibody, Cancer Immunol. Immunother. 72 (7) (2023) 2029–2044.